Sparse 2-D PZT-on-PCB Arrays With Density Tapering

Wei, Luxi; Boni, Enrico; Ramalli, Alessandro; Fool, Fabian; Noothout, Emile; Van Der Steen, Antonius F.W.; Verweij, Martin D.; Tortoli, Piero; De Jong, Nico; Vos, Hendrik J.

DOI
10.1109/TUFFC.2022.3204118

Publication date
2022

Document Version
Final published version

Published in
IEEE Transactions on Ultrasonics, Ferroelectrics, and Frequency Control

Sparse 2-D PZT-on-PCB Arrays With Density Tapering

Luxi Wei, *Member, IEEE*, Enrico Boni, *Senior Member, IEEE*, Alessandro Ramalli, *Senior Member, IEEE*, Fabian Fool, *Graduate Student Member, IEEE*, Emile Noothout, Antonius F. W. van der Steen, *Fellow, IEEE*, Martin D. Verweij, *Member, IEEE*, Piero Tortoli, *Life Fellow, IEEE*, Nico de Jong, *Member, IEEE*, and Hendrik J. Vos, *Member, IEEE*

***Abstract*— Two-dimensional (2-D) arrays offer volumetric imaging capabilities without the need for probe translation or rotation. A sparse array with elements seeded in a tapering spiral pattern enables one-to-one connection to an ultrasound machine, thus allowing flexible transmission and reception strategies. To test the concept of sparse spiral array imaging, we have designed, realized, and characterized two prototype probes designed at 2.5-MHz low-frequency (LF) and 5-MHz high-frequency (HF) center frequencies. Both probes share the same electronic design, based on piezoelectric ceramics and rapid prototyping with printed circuit board substrates to wire the elements to external connectors. Different center frequencies were achieved by adjusting the piezoelectric layer thickness. The LF and HF prototype probes had 88% and 95% of working elements, producing peak pressures of 21 and 96 kPa/V when focused at 5 and 3 cm, respectively. The one-way −3-dB bandwidths were 26% and 32%. These results, together with experimental tests on tissue-mimicking phantoms, show that the probes are viable for volumetric imaging.**

***Index Terms*— Three-dimensional (3-D) imaging, two-dimensional (2-D) array, matrix array, PZT-on-printed circuit board (PCB), sparse array, transducer, ultrasound (US), volume imaging.**

I. Introduction

VOLUMETRIC ultrasound (US) imaging based on two-dimensional (2-D) arrays is taking its position within the clinical and experimental areas due to the ability to visualize three-dimensional (3-D) structures and dynamics. Fully populated 2-D arrays can contain thousands of elements to cover a relatively large aperture [1], [2]. Multiple US research scanners can be synchronized to drive such arrays, but the hardware and software requirements make the clinical application impractical [1], [3], [4], [5], [6]. Application specific integrated circuits (ASICs) can also be used for in-probe subaperture beamforming [7], [8]. In this case, the probes can operate at high frame rate but are generally designed for specific applications and therefore are less versatile in terms of implementable scan sequences. More complex read-out sequences are used in the row–column arrays [9], [10], [11], [12]. These arrays have relatively high resolution, but multiple transmit events are required to construct a volume with a field of view limited by the transducer aperture size [13].

A tradeoff between resolution, contrast, volume rate, and imaging depth is offered by sparse arrays [14], [15], [16], [17], in which the acoustic elements sparsely cover the overall probe aperture, which can be as large as needed to achieve the desired spatial resolution. Ramalli *et al.* [18] proposed to arrange the elements of a sparse 2-D array in a tapering spiral pattern. In this design, 256 elements enable one-to-one connection with current US open scanners [19]. The spatial density of the elements is modulated according to a tapering function, acting like a physical apodization function [18]. When focused beams are used for high-resolution scanning, the frame rate can be increased due to multiline transmissions [20], [21]. Plane or diverging wave transmissions can also be used to further increase the volume rate, but angular compounding and advanced beamforming techniques are needed to increase the image quality [22]. The sparse spiral array allows the transmission sequence to be flexibly adapted to different imaging purposes and thus represents a robust option for 3-D imaging. A CMUT version of a sparse spiral array has previously been manufactured, characterized, and assessed for diverging wave volumetric imaging [23], [24].

In this article, we describe the design, fabrication, characterization, and imaging test of two sparse spiral arrays using methods that are feasible in a laboratory environment. Previous studies have described various ways to build 2-D transducers for 3-D imaging [7], [25], [26], [27], [28], [29], [30], [31]. Bulk piezoelectric (PZT) material is the most popular and established choice for building transducer elements. Building

Manuscript received 15 July 2022; accepted 30 August 2022. Date of publication 6 September 2022; date of current version 27 September 2022. This work was supported in part by the Dutch Research Council (NWO) through the Research Program "Vernieuwingsimpuls—Vidi 2017" under Project QUANTO-16572, in part by the Electronics Components and Systems for European Leadership (ECSEL) Joint Undertaking through the Moore4Medical Project under Grant H2020-ECSEL-2019-IA-876190, and in part by the Italian Ministry of Education, University and Research (PRIN 2020) under Grant 20205HFXE7. *(Corresponding author: Luxi Wei.)*

Luxi Wei is with the Department of Cardiology, Erasmus MC University Medical Center, 3000 CA Rotterdam, The Netherlands (e-mail: l.wei.@.erasmusmc.nl).

Enrico Boni, Alessandro Ramalli, and Piero Tortoli are with the Department of Information Engineering, University of Florence, 50139 Florence, Italy.

Fabian Fool and Emile Noothout are with the Department of Imaging Physics, Delft University of Technology, 2628 CJ Delft, The Netherlands.

Antonius F. W. van der Steen, Martin D. Verweij, Nico de Jong, and Hendrik J. Vos are with the Department of Cardiology, Erasmus MC University Medical Center, 3000 CA Rotterdam, The Netherlands, and also with the Department of Imaging Physics, Delft University of Technology, 2628 CJ Delft, The Netherlands.

Digital Object Identifier 10.1109/TUFFC.2022.3204118

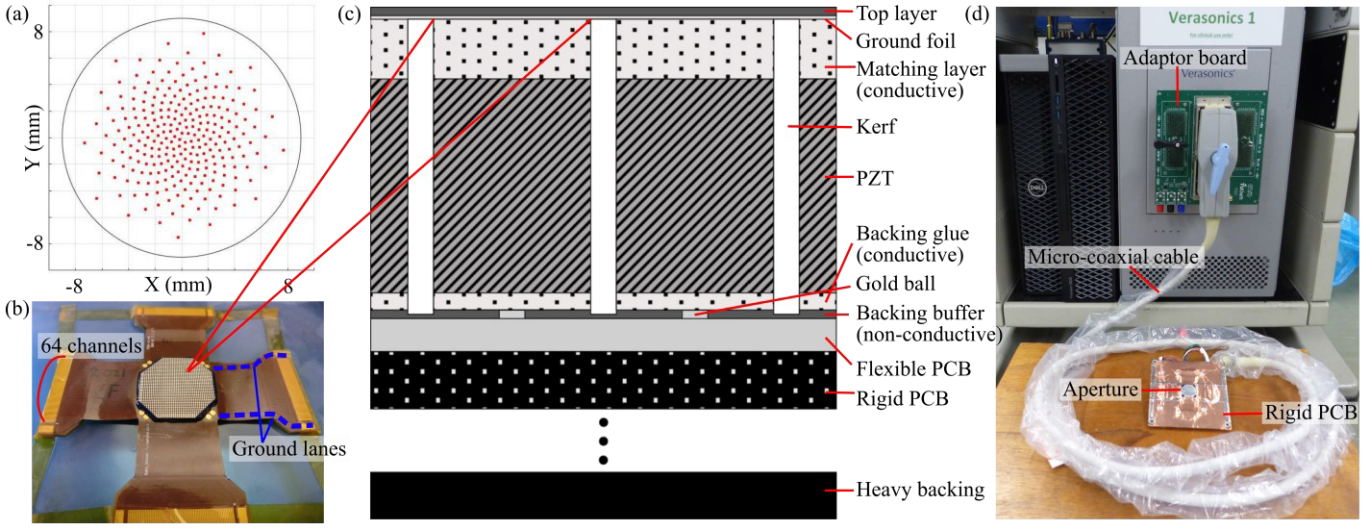

Fig. 1. (a) Proposed element locations of the sparse spiral layout. (b) Top view of the diced 2.5-MHz probe surface without the matching layer, ground foil, or top layer. The probe contained fully populated elements, but only the elements at the designed locations were electrically connected. Four flexible arms each with 64 channels and 2 ground lanes are connected to the transducer. (c) Layers inside each element/stack. (d) Fully assembled transducer on a 10 × 10 cm^2 rigid PCB connected to the US machine.

PZT 2-D transducer arrays involves depositing layers at the front of the element to acoustically match the high-impedance PZT material to tissue, as well as designing the back of the array to include proper backing impedances and electronic circuitry. The design of the electrical circuitry of the 2-D array is nontrivial because of the high demand on fan-out, as opposed to 1-D arrays. For instance, row–column arrays' elements were electrically connected with a flexible circuit that also acts as a matching layer and is further connected to printed circuit boards (PCBs) on the sides of the array [10]. This method relies on the material properties of the flexible circuit and limits the choice of front matching material. ASICs-based transducers use as a backing layer either the ASICs themselves [32] or have additional backing layers in front of the ASICs [31]. By implementing additional backing layers, the transmit efficiency may improve. For simplification of the fabrication process, Linsey *et al.* [33] have shown that PZT elements can be constructed directly on top of a thin and flexible PCB. Eames and Hossack [28] have also shown direct construction of PZT elements on a rigid PCB, with or without an intermediate backing layer.

For our sparse spiral arrays, we have chosen to build the PZT elements directly on top of a combined rigid/flex PCB for manufacturing simplicity. The PZT-on-PCB design allows fast and easy prototyping of the transducer array by allowing the selection of the active elements by using the PCB traces themselves. The rigid parts of the PCB ensure mechanical stability, whereas the flexible parts allow incorporating the array into a convenient probe casing in a subsequent step. The PZT-on-PCB method can achieve bandwidths sufficient for fundamental mode imaging. We have previously used a 5-MHz sparse spiral array for microbubble imaging [22], but in the current study, we describe the hardware design and provide the characterization of the imaging system in detail. Here, we present, for the first time in detail, an imaging system including two tapering spiral sparse 2-D arrays with PZT elements. The low-frequency (LF) probe was designed to be centered at 2.5 MHz, aimed at cardiac imaging. The high-frequency (HF) probe was designed to be centered at 5 MHz, potentially for vascular imaging.

TABLE I
SUMMARY OF PROBE DIMENSIONS

	LF probe	HF probe
Aperture diameter	1.6 cm	1.6 cm
Total elements	37×37	73×73
Active elements	256	256
Pitch	430 µm	215 µm
Minimum active pitch	430 µm	304 µm
Kerf	60 µm	20 µm
Element width	370 µm	195 µm
Element height	500 µm	225 µm
Element width-to-thickness ratio	0.74	0.87

II. TRANSDUCER DESIGN AND FABRICATION

The distribution of the 256 elements was based on a density-tapered spiral geometry. The element positions proposed by Ramalli *et al.* [18] were snapped onto a 215 × 215 μm^2 grid to enable conventional transducer dicing [Fig. 1(a) and (b)]. The final elements have the lateral dimensions of 195 × 195 μm^2 (kerf = 20 μm) for the HF array and 370 × 370 μm^2 (kerf = 60 μm) for the LF array [34]. A summary of the array and element dimensions can be found in Table I.

As detailed in Fig. 1(c), nine different layers (including matching and backing layers) contribute to each transducer element, with an additional flexible polyimide PCB layer in between the backing layer and the rigid PCB.

The thickness of each layer was varied in finite element simulations (PZFlex release 4.0, Weidlinger Associates Inc., Mountain View, CA, USA) to find a good tradeoff between

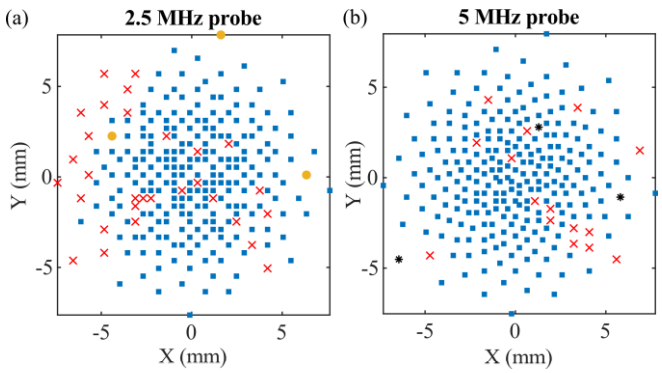

Fig. 2. Element functionality of (a) 2.5- and (b) 5-MHz probe. Most of the elements were functioning at similar levels (blue squares). Some elements were nonfunctional (red cross), had low sensitivity (black star), or had high sensitivity (yellow circle). Element sizes are not to scale.

the frequency response, time response, and transmit pressure. The simulations were performed in 3-D. A group of 11 × 11 elements were simulated, but only the central one was electrically active. The nonactive elements surrounding the element of interest were included to give a more accurate representation of the surrounding interactions. During the simulation process, high bandwidth and low-ringing behavior were considered because of their relationships with image quality. Tables I and II contain the final layer thickness values and material properties. The values for silicone rubber, aluminum, CT S3203 HD, gold, FR4, and 25% tungsten-loaded epoxy were provided by the simulation software; the other values were measured in house or obtained from literature.

The probes were built as PZT-on-PCB, partly expanding on our earlier PZT-on-ASIC technology described for a micro-transesophageal matrix transducer [32]. During the manufacturing process, a fully populated rectangular grid of elements was cut, but only 256 elements were electronically connected to the PCB by gold balls [see Fig. 1(c) for a schematic of the stack and Fig. 2 for the element pad locations]. The elements with positions closer to the ideal ones were selected: the maximum distance between the effective and the ideal element positions was estimated to be less than 250 and 100 μm for the LF and HF probes, respectively.

The electrical connections were implemented by PCB conductive traces between the 256 element pads and the bondable pads on the tip of four arms. Each arm thus contains 64 element connections and holds two 1.5-mm-wide ground lanes [Fig. 1(b)]. This PCB design was realized in high-precision rapid prototyping PCB technology (RushPCB, San Jose, CA, USA), with a rigid base thickness of 1.49 mm, a polyimide [35], [36] flex print of 77-μm glued on top, containing copper traces of 7-μm thickness. This type of flex print allows for a minimum of 65-μm trace width and spacing. Gold balls (diameter $\approx$ 50 μm) were applied on top of the PCB element pads. A nonconductive epoxy was poured between the gold balls to form the substrate to the elements. After curing, this layer was ground down to expose the gold balls, forming electrical contact points for the PZT stack. Next, the high-density piezoceramic (3202HD, CTS Corporation) layer of appropriate thickness was glued onto the nonconducting buffer using an electrically conductive paste (silver-filled two component epoxy). The conductive paste was also applied on the back side to provide electrical connection between the PZT and the exposed gold balls. The same conductive glue was applied to the front side of the PZT to form an acoustical matching layer. The thickness of the layers was controlled by using molds, and postcure at 70 °C was performed. The stack was then cut with a conventional dicing saw down to the nonconductive buffer layer, creating a rectangular grid of elements [Fig. 1(b) and (c)]. The nonconductive epoxy also acted as a mechanical dicing buffer layer as well as electrical isolation. On the front side, a thin conductive aluminum foil (ground foil) was attached. The electrically conductive glue was applied to the ground foil and raked. Then, the ground foil was rubbed on the matching layer, which ensured electrical glue contact of each element, resulting in a homogeneous layer without air bubbles. The aperture was then covered with a thin layer of silicone rubber for protection of the ground foil, and the stack with the flexible PCB was mounted on a regular-process rigid PCB [EuroCircuit, Mechelen, Belgium; Fig. 1(d)]. Finally, for the LF probe only, an attenuating backing layer was attached to the backside of the PCB to prevent further ringing. The backing layer was not included in the simulations, but instead, an absorbing boundary condition was placed behind the PCB to reduce the simulation duration. The material impedance can be found in Table II.

III. Transducer Characterization and Imaging Methods

Preamplifiers, as described by Boni *et al.* [37], were used to amplify the received signals and to buffer the high impedance elements, thus reducing the attenuation by the cable load and increasing the overall signal-to-noise ratio. The probes were connected to a Vantage-256 scanner (Verasonics, Kirkland WA) via a 2-m-long microcoaxial cable and a PCB adaptor board, both custom-designed and built. Fig. 1(d) shows the LF prototype array connected to the Vantage system.

The acoustic characterization of single elements and the full probe was performed in water. The element viability was measured in pulse-echo mode using a polyoxymethylene block 7 cm thickness and placed 3 cm away from the probe surface.The 256 elements sequentially transmitted and received, and the peak echo amplitudes across all elements were measured. The median across all elements was used as the comparison value. We classified the element viability into four groups relative to the median amplitude: nonfunctional (< -20 dB), low amplitude (> -20 dB and < -12 dB), normal (> -12 dB and <12 dB), and high amplitude (>12 dB).

To determine the time and frequency behavior of the elements, a 200-μm-diameter polyvinylidene flouride (PVDF) needle hydrophone (Precision Acoustics, Dorchester, U.K.) was placed 1 cm away from the centers of the transducers. Each element was excited by 1-cycle and 4-cycle Gaussian-modulated sinusoidal pulses at the center frequencies of the two probes (2.5 and 5 MHz). The 16 consecutive pulses collected by the hydrophone were averaged. The pulses received from all elements were lined up by cross correlation to remove

TABLE II
LAYER COMPOSITION, DIMENSIONS, AND MATERIAL PROPERTIES

Layers	Material	Properties	Thicknesses, LF probe (μm)	Thicknesses, HF probe (μm)
Top layer	silicone rubber	ρ = 1294 kg/m^3, c_b = 1022 m/s, c_s = 125 m/s	15	15
Ground foil	aluminum	ρ = 2690 kg/m^3, c_b = 6306 m/s, c_s = 3114 m/s	7	7
Matching layer	conductive epoxy	ρ = 3330 kg/m^3, c_b = 1873 m/s, c_s = 970 m/s	140	60
PZT	CTS 3203 HD	c11 = c22 = 1.4e11, c12 = 8.8e10, c13 = c23 = 9.2e10, c33 = 1.3e11, c44 = c55 = 2.2e10, c66 = 2.5e10 N/m^2 e15 = e24 = 16, e31 = e32 = –9, e33 = 22 C/m^2 ε11 = ε22 = 1306, ε33 = 1200	500	225
Backing glue	conductive epoxy	same as above	40	40
Backing buffer	non-conductive epoxy	ρ =3350 kg/m^3, c_b = 2000 m/s, c_s = 1050 m/s	20	20
Electrical pad	gold	ρ =19700 kg/m^3, c_b = 3240 m/s, c_s = 1200 m/s	20	20
Flexible PCB	polyimide	ρ = 1420 kg/m^3, c_b = 2246 m/s, c_s = 1105 m/s	77	77
Rigid PCB	FR4	ρ = 1850 kg/m^3, c_b = 3602 m/s, c_s = 2396 m/s α_b = 3, α_s = 3 dB/MHz/cm	1490	1490
Heavy backing	tungsten-loaded epoxy	(not included in simulations) ρ = 3710 kg/m^3, c_b = 1800 m/s, α_b = 15 dB/MHz/cm	0	>1e6

ρ: density, c_b: bulk velocity, c_s: shear velocity, c: stiffness constant, e: piezoelectric coupling constant, ε: dielectric constant, α_b: bulk attenuation, α_s: shear attenuation

any element-hydrophone time of flight variation and then averaged to obtain the average probe signal. The time and frequency responses were calculated and compared with the simulated results. The ringing to main lobe amplitude ratio (RMR) was calculated based on the following equation:

$$\mathrm{RMR} = 20 \times \log_{10}\left(\frac{\mathrm{Max}\left(\mathrm{envelope}_{\mathrm{ringing}}\right)}{\mathrm{Max}(\mathrm{envelope})}\right). \quad (1)$$

The main lobe durations [shown in gray in Fig. 3(a) and (b)] were determined using the approximated transmit pulse from the Verasonics software.

The achievable acoustic pressures were also determined. The LF and HF probes were used to transmit unsteered beams, focused at 5- and 3-cm depths, respectively, and the peak pressures were measured using 1-mm and 200-μm hydrophones (Precision Acoustics, Dorchester, U.K.) at the focal depths.

The grating lobe levels and angular transmit profile were assessed for both probes using the 200-μm hydrophone. The field of the HF array was measured as described in [34] with the probe mounted on a rotating stage and the fixed hydrophone pointing toward the probe for all angles. The field of the LF array was measured by moving the hydrophone over a circular arc within ±60° with 0.5° increments at the focal depth without rotating either the probe or the hydrophone needle. The reduction in received pressure due to hydrophone opening angle was estimated based on [38] and correspondingly corrected. Angle correction was not necessary for the 5-MHz probe since the probe was rotated during the measurements, such that the needle faced the direction of the transmit beam at all angles [34].

Seven focusing angles were measured. The beams for the LF probe were steered between ±30° on the *XZ* plane in steps of 10°. The HF probe was steered to ±45° on the *XZ* plane in steps of 15° [34]. The peak voltage received at each steering angle was recorded and normalized to the value obtained at 0° steering. A polynomial fit of the measured peak amplitude versus steering angle was performed, and opening angles were calculated at the −6 dB level. Field II simulations were also performed as a comparison.

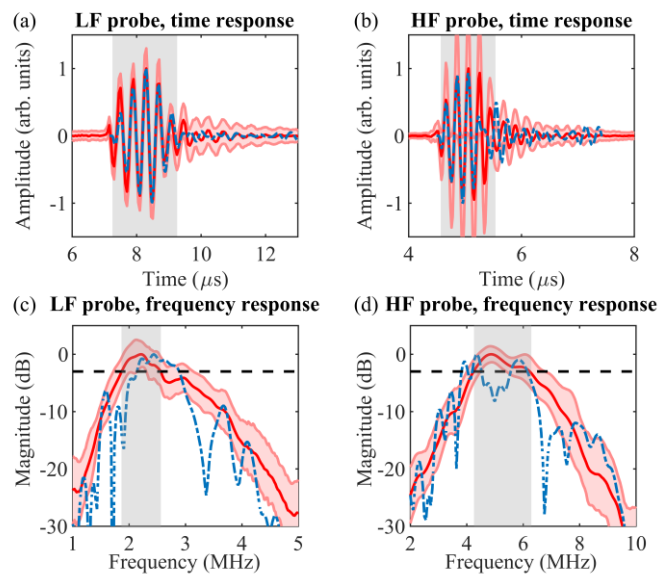

Fig. 3. (a) and (b) Time and (c) and (d) frequency responses of (a) and (c) LF and (b) and (d) HF probes in simulation (blue dashed) and from hydrophone measurements (red, ±standard dev). (a) and (b) Gray shaded time segments indicate the main lobe duration used to calculate ringing to main lobe ratio. (c) and (d) −3 dB level (black dashed) was used to assess the bandwidths of the probes. The gray shaded frequency segments indicate the bandwidths of the probes. The 4-cycle transmit pulses were used for (a) and (b) and 1-cycle transmit pulses were used for (c) and (d).

To demonstrate the achievable resolution and depth, both probes were used to image the cross planes of a tissue-mimicking resolution phantom (040-GSE, CIRS, Norfolk, VA, USA). The LF and the HF probes transmitted 3-cycle

pulses (with amplitude equalization) at the respective center frequencies, focused at 5- and 3-cm depths, respectively. Each image was reconstructed, on both *XZ* plane and *YZ* plane, by scanning with 40 focused beams across a 40° field of view. Beamforming was performed using the Verasonics delay-and-sum beamformer at a pixel size of $0.5 \times 0.5\lambda$ for both arrays. The imaging depth for both cases was 12 cm. The 18 frames were averaged to reduce the effects of electronic noise. Field II simulations were also performed with the same transmit parameters, and single scatterers located at the same depths of the phantom wires. Depths between 3 and 12 cm were assessed for the LF probe, and 3 and 6.5 cm were assessed for the HF probe. Theoretical axial and lateral FWHM values were calculated at the focus

$$\mathrm{FWHM}_{\mathrm{axial}} = 0.5 \cdot \lambda \cdot N \tag{2}$$

$$\mathrm{FWHM}_{\mathrm{lateral}} \approx \frac{\lambda}{A} \tag{3}$$

where λ is the wavelength, N is the number of cycles, and A is the effective aperture size [39], [40]. Axial FWHM values were in units of mm, whereas lateral FWHM values were in units of radians. Because of the density taper, the effective aperture size was 7.5 mm [18].

To assess the clutter level, the same cross-plane imaging sequence was used to image a tissue-mimicking polyvinyl acetate phantom having a 1-cm-diameter cylinder filled with water (Fig. 6). The phantom was placed in a water tank 2 cm away from the probe surface. The beams were focused at 5 cm, and the receiver gain levels were kept constant through depth. The 3-D Field II simulations were also performed for a comparison. A $3 \times 3 \times 2$ cm^3 block was homogeneously filled with ten point scatterers per resolution cell [41]. The simulation imaging parameters were kept the same as in the phantom experiment. The contrast difference of the hypoechoic and tissue regions (CTR) was calculated using the following equation on two region of interests (ROIs) manually selected, as shown in Fig. 6:

$$\mathrm{CTR} = 20 \times \log_{10}\left(\frac{\mathrm{rms(hypoechoic\ region)}}{\mathrm{rms(tissue\ region)}}\right). \tag{4}$$

To further distinguish clutter and grating lobes due to element location design or hardware implementation, Field II simulations of the sparse LF probe were performed using the measured impulse response function (IRF) and a simulated IRF (1 cycle sinusoid with a Hanning window), as well as a fully populated probe with the same dimensions. The simulations were performed for a focused-beam steered by 28°, and the transmitted beams were assessed over an arc spanning the range [−60, 60]°.

IV. Results

Table III provides a summary of all experimental and simulation results.

The element viability was derived from the pulse-echo experiment. Fig. 2 indicates the locations of the elements and highlights the positions of nonworking ones. The yield of the two arrays was 88% and 95% (>−20 dB) for the LF and HF probes, respectively. For the LF probe, 30 elements were nonfunctional, and three elements had overly high amplitudes. Part of the nonfunctional elements was concentrated on one edge of the array, which may lead to degradation in resolution. For the HF probe, three elements had low amplitudes and 15 elements were nonfunctional.

Fig. 3 shows the experimental single-element time and frequency responses compared to simulations. The measured center frequency and (−3 dB one-way) bandwidth of the LF probe were 2.2 ± 0.2 and 0.6 ± 0.3 MHz (26% ± 13%), respectively. For the HF probe, the measured center frequency was 5.0 ± 0.5 MHz, the same as the expected one. The measured (−3 dB one-way) bandwidth was 1.6 ± 0.6 MHz (32% ± 11%). A dip around 5 MHz in the frequency spectrum of the simulation result can be observed. The 4-cycle temporal responses of both probes were qualitatively similar to the simulations. The RMR of the LF probe was calculated to be −15 and −12 dB for simulation and experiment, respectively. Similarly for the HF probe, the results were −6 and −10 dB for simulation and experiment, respectively.

The peak positive pressures and transmit efficiencies were measured by the hydrophone when transmitting a focused beam without steering. Relative to the driving voltage of the Vantage 256 system, the probes generated peak positive pressures of 21 kPa/V (LF, 5-cm depth) and 96 kPa/V (HF, 3-cm depth).

Fig. 4 shows the relative pressures detected when the US focused beams were steered in the *XZ* plane. For both probes, the background signal, which consists of clutter in the transmit field and stochastic noise of the system, was below −22 dB. While the HF probe does not have pronounced grating lobes when steered up to 45°, grating lobes of up to −20 dB can be seen when steering the LF probe at ±30°. The peak transmit pressure decreased with increasing steering angles due to the opening angle of the elements. The opening angles of the two probes, measured as the −6 dB width of the main beam of a single element, were 62° and 81° for the LF and HF probes, respectively. The experimental opening angle of the LF probe was lower than in simulation (128°), while for the HF probe, the results were comparable (80°). The characteristics of the unsteered beam are further discussed in the Appendix.

Fig. 5 shows the phantom cross-plane images obtained using the two arrays. Considering the grating lobes visible in Fig. 4 and the size of the phantom, the maximum steering angle was limited to 20° in all cases. Both arrays were able to resolve the point scatterers on the *XZ* plane as well as the hyperechoic cylinder on both cross planes. As expected, the LF array could reach a deeper imaging depth (at least 12 cm) but had a worse resolution compared to the HF array. Quantitative comparison of the full-width at half-maximum (FWHM) in both axial and lateral directions between the experimental and simulated results is listed in Table III. From the Field II simulations, axial resolutions were determined to be 1.52 ± 0.06 and 0.63 ± 0.01 mm for the LF and HF probes, respectively, and lateral resolutions were 0.06 ± 0.02 and 0.04 ± 0.01 radians for the LF and HF probes, respectively. The experimental axial resolution results were 1.70 ± 0.25 and 0.74 ± 0.06 mm for the LF and HF probes, and in the lateral direction 0.08 ± 0.01 and 0.04 ± 0.01 radians

TABLE III
SUMMARY OF RESULTS

	LF probe		HF probe	
	Simulation	Experiment	Simulation	Experiment
Lateral resolution (rad)	0.06 ± 0.02 (depth range: 3 - 12 cm)	0.08 ± 0.01 (3 - 12 cm)	0.04 ± 0.01 (depth range: 3 - 6.5 cm)	0.04 ± 0.01 (3 - 6.5 cm)
Axial resolution (mm)	1.52 ± 0.06 (3 - 12 cm)	1.70 ± 0.25 (3 - 12 cm)	0.63 ± 0.01 (3 - 6.5 cm)	0.74 ± 0.06 (3 - 6.5 cm)
Yield		88%		95%
Opening angle (°)	128°	62°	80°	81°
Hypo-echoic CTR	−53 dB	−14 dB	−40 dB	−9 dB
f_0	2.5 MHz	2.2 ± 0.2 MHz	5.4 MHz	5.0 ± 0.5 MHz
Bandwidth	30%	26% ± 13%	46%*	32% ± 11%
Transmit efficiency (focused beam)		21 kPa/V (@ 5 cm depth)		96 kPa/V (@ 3 cm depth)
RMR	−15 dB	−12 dB	−6 dB	−10 dB

*calculated at the widest -3 dB crossings (ignoring dips in the center of the frequency spectrum)

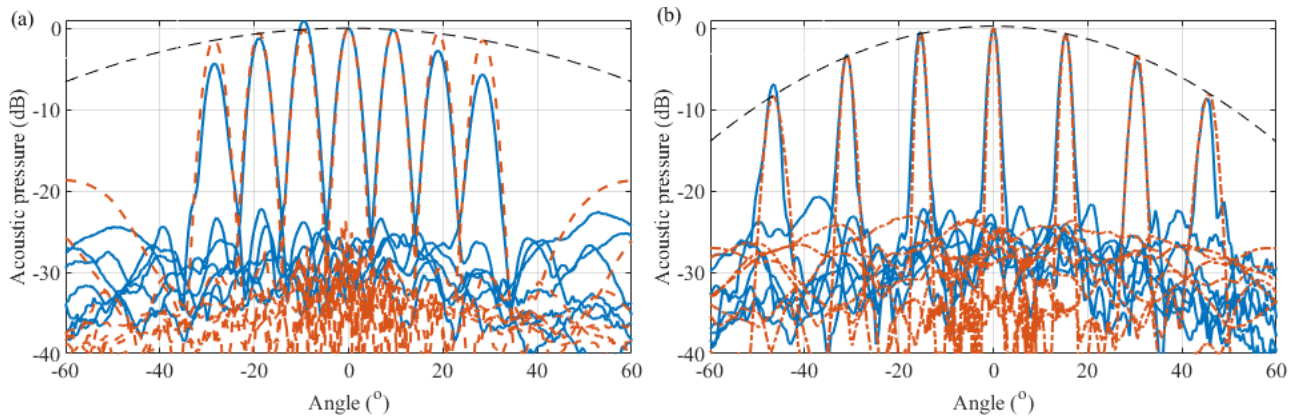

Fig. 4. Measured focused beam profiles when steering between ±30° and ±45° for (a) LF and (b) HF probes, respectively. For the LF probe, the hydrophone sensitivity angle was corrected. For the HF probe measurement, the probe was always rotated, such that the hydrophone needle faced the direction of the transmit beam. The dashed curve is a polynomial fit of the simulated peak amplitudes. The clutter (below −20 dB) is mainly due to the sparsity of the elements and crosstalk between elements.

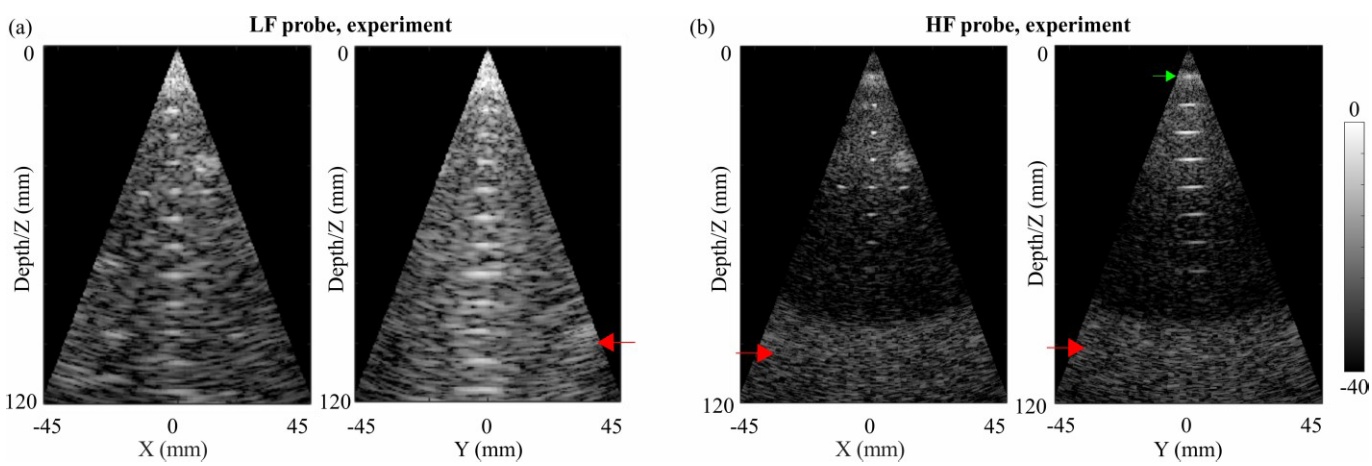

Fig. 5. (a) and (b) Focused beam imaging of the cross planes of the tissue-mimicking resolution phantom for both probes. Artifacts caused by grating lobes coming from the edge of the phantom can be seen for both arrays (red arrows).

for the LF and HF probes, respectively. Theoretical values were also calculated using (2) and (3). They were 1.23 and 0.62 mm for the axial FWHMs of the LF and HF probes, respectively, and 0.08 and 0.04 radians for the lateral FWHMs of the LF and HF probes, respectively. Theoretical lateral FWHMs were calculated based on an effective aperture size of 7.5 mm. The experimental results showed larger FWHMs in both axial and lateral directions compared to the simulated and theoretical results. Some artifacts could be seen (Fig. 5, red arrows) and were likely due to grating lobes receiving the

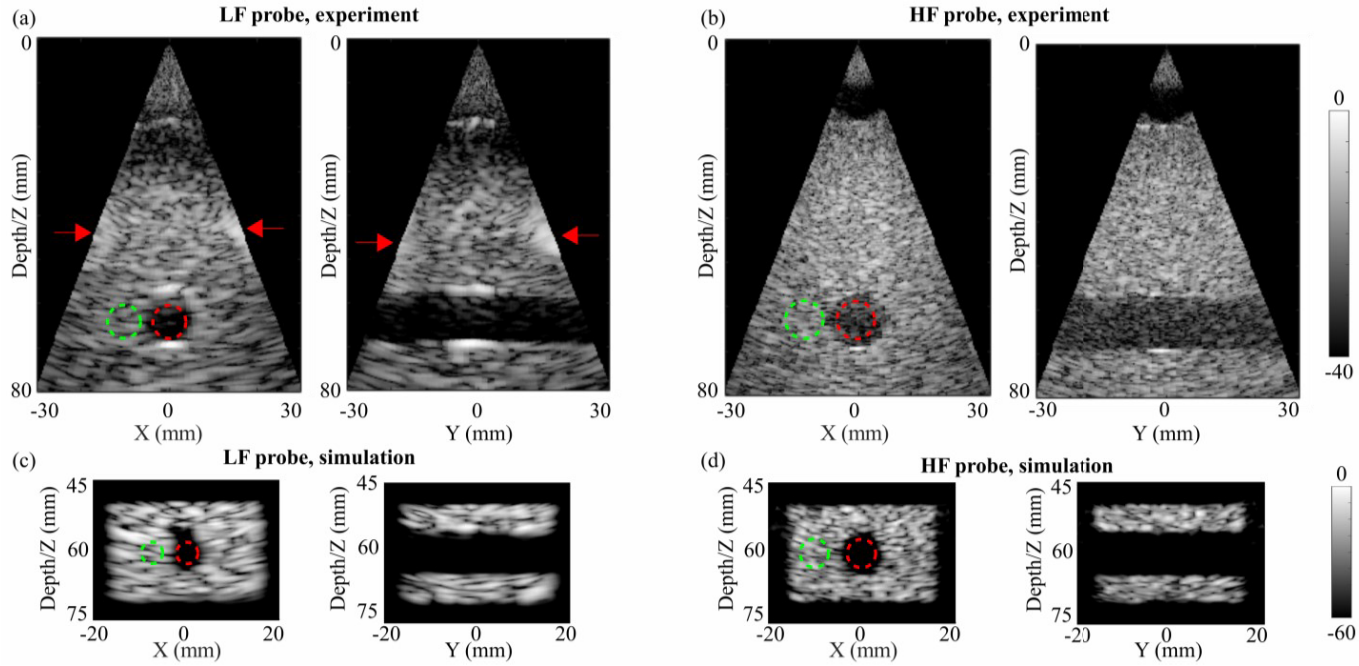

Fig. 6. Experimental (a, b) and simulated (c, d) focused beam images of a hypoechoic cylinder inside a tissue-mimicking phantom. CTR values were calculated using the hypoechoic region (red circles) and the tissue region (green circles). Artifacts due to grating lobes receiving echoes from the water tank wall could be seen on the edges of the image in (a) (red arrows).

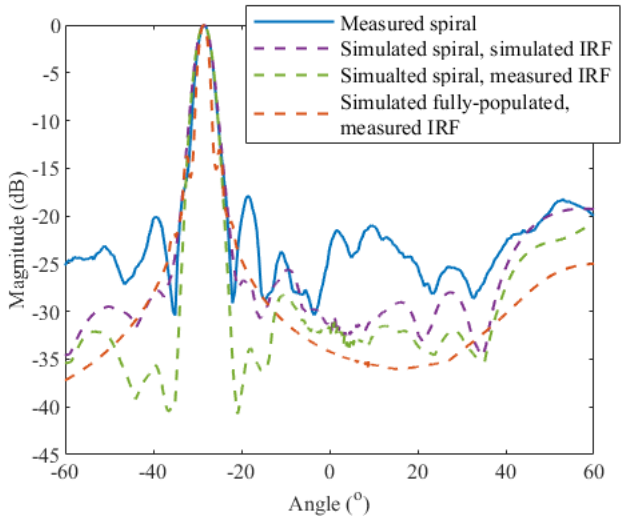

Fig. 7. Transmit field angular profiles of a focused beam at 28° steering angle. The hydrophone measurement of the HF spiral (blue) is displayed alongside the profile of a simulated HF spiral using the measured IRF and simulated IRF (purple and green dashed lines). An imaginary fully populated array of the same aperture size was also simulated for comparison (orange dashed line).

echoes from the edge of the phantom. There was also a water bag placed between the probe and the surface of the phantom for acoustic coupling, and the reflections from the water to phantom interface can be seen on the images (Fig. 5, green arrow).

Fig. 6 shows the results of clutter assessment both in simulation and with a phantom. In simulation, CTR values between the hypoechoic region and the tissue region were −53 and −40 dB for the LF and HF arrays, respectively. In the experiment, the CTR values for these probes were −14 and −9 dB. Some artifacts due to grating lobes receiving echoes from the water tank wall could be seen on the edges of the image for the LF probe [Fig. 6(b), red arrows]. Fig. 7 shows the comparison of the transmit field obtained in simulations and experiments at a transmit angle of 28°. The clutter level was the highest for the measured beam and the lowest for a fully populated probe. The measured clutter level was higher compared to the simulated sparse arrays, when using either the simulated or the measured IRFs.

V. Discussion

In this article, we have presented the design, realization, and characterization of two sparse spiral arrays, built on PCBs for fast prototyping.

The 12% and 5% of the elements were found to be nonfunctional for the LF and HF arrays, respectively. The elements could be nonfunctional due to manufacturing errors that led to loss of electrical connection inside or outside of the stacks, layer detachment, or overdicing. Overdicing into the PCB could lead to multiple electrical traces being cut, resulting in a cluster of nonfunctioning elements. This could explain the top left cluster of nonfunctional elements in the LF array [Fig. 2(a)]. The variation in the elements' transmit pressures and receive sensitivities could be due to variabilities in layer thicknesses caused by uncertainties in the layer deposition process. The high sensitivity of some elements could also be originated by incomplete dicing between adjacent active and passive elements, doubling the surface area of the active element. In this case, an increase in transmit and receive

sensitivity may be expected, but this will also result in a reduced opening angle.

Fig. 3 shows the comparison between simulated and measured frequency and time responses of elements. The center frequencies of the simulated and realized probes were 2.5 and 2.2 ± 0.2 MHz for the LF probe and 5.4 and 5.0 ± 0.5 MHz for the HF probe, quite close to the designed ones of 2.5 and 5 MHz. The frequency spectrum of the simulated HF probe had a drop in amplitude in the center of the passband due to the flexible PCB layer. Experimentally, this behavior was not observed. The difference could be due to material property definition for the simulation or layer thickness uncertainties. This dip in amplitude also led to the low RMR (high amplitude ringing) for the simulation (−6 dB) compared to the experiment (−10 dB). Low RMR values correspond to worse axial resolution, which also explains the worse measured axial FWHM compared to the simulated and theoretical values (Table III). The low RMR values could be due to lateral modes, reflections in the backing layers, and crosstalk.

The bandwidth of the LF probe agreed with the simulated results, while for the HF probe, a dip in amplitude was present around the center frequency. The bandwidth differences could be due to material property differences and/or geometry changes during the manufacturing process. In addition, simplifications in the simulations were made to reduce the computation time, which could lead to differences compared to the measurement results. The simulations were performed for a 3-D element with other nonactive elements placed next to it to form an 11 × 11 element grid. Effects from further elements were not simulated. Since, in the experiments, we did not observe any reflected pulse from the back side of the PCB/heavy backing, we only simulated a thin layer of PCB with an absorbing boundary to increase simulation speed. In practice, there could still be low amplitude waves being reflected off the back of the PCB/backing layer. Other details such as copper traces, layers within the rigid PCB, and the capped-spherical shape of the gold balls were not included in the simulations.

The bandwidths of the current probes are sufficient for fundamental mode imaging but are too low for contrast imaging at higher harmonics. The backing and matching layers contributed to the low bandwidths. The large difference in impedance of the PZT and the PCB led to strong reflections inside the PZT, which reduced the bandwidth. Furthermore, the single (front) matching layer limited the amount of impedance matching, creating more reflections inside the stack. While the PCB backing is a part of the design and can be just residually changed, the acoustic matching can be improved to accommodate a wider frequency range. Commercial probes often have more than one matching layer to improve acoustical matching [42]. Subdicing of the elements can also further separate the thickness and width resonance modes [28], possibly leading to higher bandwidths and less ringing. Composite PZT or single crystal technologies can further increase the bandwidth of the probe by increasing the efficiency of the electrical–mechanical coupling [43], [44]. The possible use of multiple matching layers or other PZT materials will be a part of our future work.

The transmit efficiency was higher for the HF array than for the LF array focused at their target depths. Because of the lower center frequency and greater focal depth, the focal diameter of the LF array was larger than that of the HF array. That means if the output pressures from the probes were the same, the same energy was distributed onto a larger area at LF, leading to a lower peak pressure. The transmit efficiency can be increased by introducing multiple matching layers to achieve better impedance matching of PZT to water/tissue or to use matching coils for every element. These are used in commercial probes but are not included in the current design. The received signal-to-noise ratio is also improved by the addition of in-probe preamplifiers [37]. Overall, the current transmit efficiency is sufficient for phantom imaging at a reasonable driving voltage amplitude (30 V). A 50-V peak voltage has been used in other experiments without noticeable damage to the probes.

The originally designed elements' locations based on the tapering Fermat's spiral pattern were changed to their closest grid locations. The 2-D grid simplified the manufacturing process, allowing dicing saws to be used. For the HF array, the layout still resembled the original grid-less design, but due to the large element size of the LF array, the central area of the LF probe almost approached that of a fully populated array. The drawback is that higher grating lobe levels can be expected because of this repeating grid pattern. This is also what we observed in Fig. 4, higher grating lobes appeared as the beams were steered. Grating lobes as well as overall clutter will degrade image quality in delay-and-sum beamformed images. By reducing the transmit and receive angles and by using coherence-based beamforming, grating lobes and clutter can be suppressed [22].

Fig. 4 also shows agreement between the measured and calculated opening angle of the HF probe when transmitting focused beams, while for the LF probe, the measured opening angle was narrower than expected. One possibility is that the effective surface area of the elements was larger in practice due to partial filling of the diced kerf. After dicing of the matching layer and PZT pillars, a thin paste of matching material was used to glue the ground foil onto the diced matching layer. The material could partially fill the kerfs, leading to an increased effective surface area. Another possibility is that crosstalk between adjacent elements through the backing layer increases the effective size of the element. The increase in the effective size of the element leads to a decrease in opening angle.

While the opening angle for the HF probe was sufficient for imaging the carotid artery, the 62° opening angle for the LF probe was low for cardiac imaging and should be improved. To increase the opening angle, smaller elements can be used. This, however, comes at a cost of transmit and receive sensitivities. Moreover, the manufacturing process becomes more difficult, as narrower PZT pillars are more likely to collapse or detach. If the sensitivity reduction can be minimized by better matching layer designs and the PZT pillars can be manufactured with high success rates, a larger opening angle (128°) can be theoretically achieved.

The experimental axial and lateral resolutions were worse, on average, than the simulation results (Fig. 5). The largest

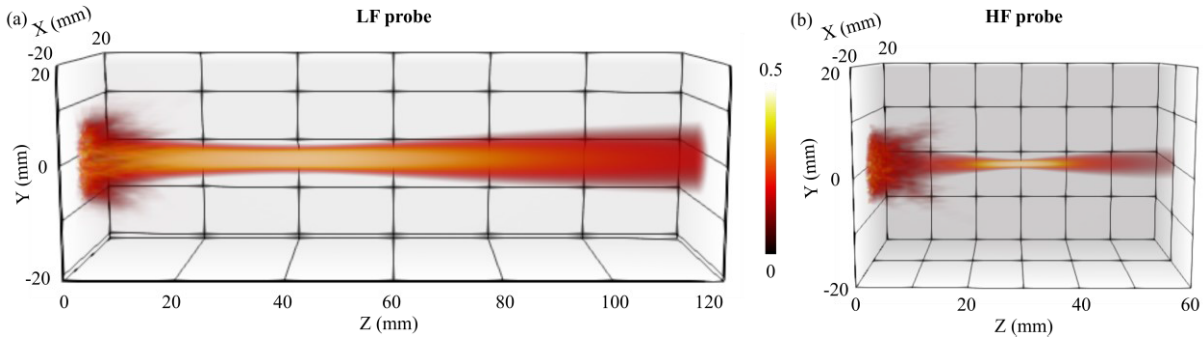

Fig. 8. 3-D Field II simulations of a beam focused at 5- and 3-cm depth for (a) LF and (b) HF probes, respectively. Amplitude of the transmit field is displayed to half the maximum value for better visualization.

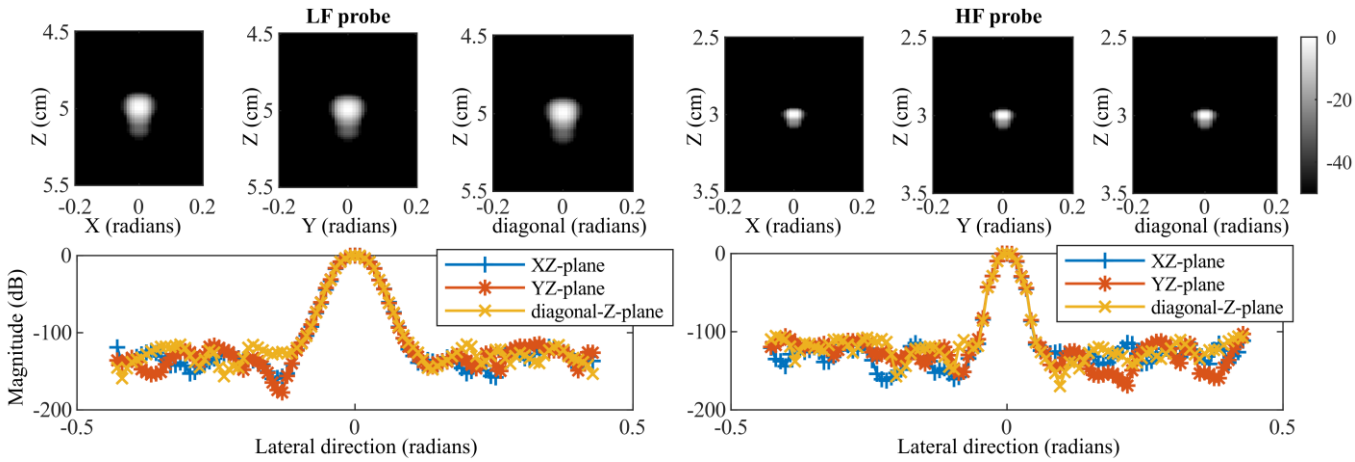

Fig. 9. Simulated single point scatterers from the *XZ*, *YZ*, as well as a *XY*-diagonal-*Z* planes.

difference was up to 50% worse. The differences could be due to variations in sensitivities and transmit pulse phase between elements, which was not included in the simulations. The theoretical axial FWHM values were lower than the values obtained in both simulation and experiments. In practice, the transmit pulses were longer than 4-cycles due to ringing and in turn higher axial FWHM values. In the lateral direction, the theoretical FWHM values were calculated considering a 7.5-mm-wide effective aperture. Theoretical lateral resolution values agreed with the experimental results. To improve the PSFs, the transmit pulse cycle number can be reduced, while smaller lateral PSFs can be achieved by increasing the size of the receive aperture. For the LF probe, meant for cardiac applications, the size of the aperture (currently 16 mm) needs to be small enough to approximately fit in between ribs. State-of-the-art clinical phased arrays also have footprints around 15 mm for this purpose. For the HF probe, the size of the aperture (currently 16 mm) could be adapted to the application requirements as often in vascular imaging the footprint is not a limitation.

The clutter level was higher in the experiments compared to the simulations (Fig. 6). This was also confirmed in Fig. 7, where a hydrophone measurement of a steered beam was compared with Field II simulations using different IRFs and a fully populated array. Since the simulated sparse array produced lower clutter than the experimental one, the sparsity of the elements could not be considered as the only cause for clutter. Reasons for high clutter levels include crosstalk between the elements, electronic crosstalk, noise of the system, and element-to-element phase and amplitude variations.

We demonstrated the penetration depths of both probes on tissue-mimicking phantoms (Fig. 5). When combined with in-probe preamplifiers for the receive signal, the probes reached 7- and 12-cm depths, which is sufficient for carotid and cardiac applications.

For these proof-of-concept probes, we have opted to use the flexible and rigid PCB layers as the backing material to decrease the complexity of the manufacturing steps. However, the poor impedance matching between the PZT and the PCB led to strong ringing, thus reducing the bandwidth of the probes. Furthermore, the low attenuation of the PCB material may have led to reflections within the PCB layer and could lead to more delayed ringing or clutter due to crosstalk. For the next designs, high impedance and high attenuation materials will be considered and placed directly behind the PZT layer to reduce these effects.

VI. Conclusion

We have built two 2-D spiral sparse arrays directly on rapid prototyping PCBs for proof-of-concept characterizations and imaging experiments. Simplicity in the stack design was preferred over complex matching and backing layer designs

to make in-house manufacturing possible. The results show that these PCB-backed probes can achieve sufficient pressures and bandwidths for phantom deep-structure imaging at the fundamental frequencies.

Appendix

Since the circular aperture and the element locations were not biased toward a specific side, the PSFs were expected to be radially symmetrical. Fig. 8 shows the 3-D simulated transmit fields focusing at 5 and 3 cm in front of the HF and LF probes. The focused beams were qualitatively radially symmetric. We performed further Field II simulations of a single scatterer positioned at 5 and 3 cm for the LF and HF probes, respectively. The *XZ* plane, *YZ* plane, and a diagonal-*Z* plane were simulated, and the FWHM of the PSF in these directions was calculated (Fig. 9). For both probes, the FWHMs in the three lateral directions are equal to the second decimal place and were 0.05 and 0.03 radians for the LF and HF probes, respectively.

Acknowledgment

The authors would like to thank Davide Galeotti, Filippo Piccardi, Andrea Traversi, and Verya Daeichin, TU Delft, Delft, The Netherlands, for their early work on the spiral array, Henry den Bok, TU Delft, for the design and implementation of the electronics, Boudewine Ossenkoppele, Djalma dos Santos, TU Delft, and Antonio Lopez Marin, Erasmus MC, Rotterdam, The Netherlands, for their help on simulations and hydrophone measurements. They would also like to thank Robert Beurskens, Erasmus MC, for the discussions and hardware support.

References

[1] J. Yu, H. Yoon, Y. M. Khalifa, and S. Y. Emelianov, "Design of a volumetric imaging sequence using a vantage-256 ultrasound research platform multiplexed with a 1024-element fully sampled matrix array," *IEEE Trans. Ultrason., Ferroelectr., Freq. Control*, vol. 67, no. 2, pp. 248–257, Feb. 2020.

[2] *Vantage Volume Datasheet*, Verasonics, Kirkland, WA, USA, 2018.

[3] B. Heiles *et al.*, "Ultrafast 3D ultrasound localization microscopy using a 32×32 matrix array," *IEEE Trans. Med. Imag.*, vol. 38, no. 9, pp. 2005–2015, Sep. 2019.

[4] L. Petrusca *et al.*, "Fast volumetric ultrasound B-mode and Doppler imaging with a new high-channels density platform for advanced 4D cardiac imaging/therapy," *Appl. Sci.*, vol. 8, no. 2, p. 200, Feb. 2018.

[5] D. Mazierli, A. Ramalli, E. Boni, F. Guidi, and Tortoli, "Architecture for an ultrasound advanced open platform with an arbitrary number of independent channels," *IEEE Trans. Biomed. Circuits Syst.*, vol. 15, no. 3, pp. 486–496, Jun. 2021.

[6] C. Risser *et al.*, "Real-time volumetric ultrasound research platform with 1024 parallel transmit and receive channels," *Appl. Sci.*, vol. 11, no. 13, p. 5795, Jun. 2021.

[7] J. Janjic *et al.*, "A 2-D ultrasound transducer with front-end ASIC and low cable count for 3-D forward-looking intravascular imaging: Performance and characterization," *IEEE Trans. Ultrason., Ferroelectr., Freq. Control*, vol. 65, no. 10, pp. 1832–1844, Oct. 2018.

[8] P. Santos, G. U. Haugen, L. Løvstakken, E. Samset, and J. D'hooge, "Diverging wave volumetric imaging using subaperture beamforming," *IEEE Trans. Ultrason., Ferroelectr., Freq. Control*, vol. 63, no. 12, pp. 2114–2124, Dec. 2016.

[9] M. Pappalardo *et al.*, "Bidimensional ultrasonic array for volumetric imaging," U.S. Patent WO2 008 083 876 A3, Sep. 25, 2008.

[10] C. H. Seo and J. T. Yen, "A 256×256 2-D array transducer with row-column addressing for 3-D rectilinear imaging," *IEEE Trans. Ultrason., Ferroelectr., Freq. Control*, vol. 56, no. 4, pp. 837–847, Apr. 2009.

[11] H. Bouzari, M. Engholm, S. I. Nikolov, M. B. Stuart, E. V. Thomsen, and J. A. Jensen, "Imaging performance for two row–column arrays," *IEEE Trans. Ultrason., Ferroelectr., Freq. Control*, vol. 66, no. 7, pp. 1209–1221, Jul. 2019.

[12] A. Sampaleanu, P. Zhang, A. Kshirsagar, W. Moussa, and R. J. Zemp, "Top-orthogonal-to-bottom-electrode (TOBE) CMUT arrays for 3-D ultrasound imaging," *IEEE Trans. Ultrason., Ferroelectr., Freq. Control*, vol. 61, no. 2, pp. 266–276, Feb. 2014.

[13] S. I. Awad and J. T. Yen, "3-D spatial compounding using a row-column array," *Ultrason. Imag.*, vol. 31, no. 2, pp. 120–130, Jan. 2009.

[14] J. Provost *et al.*, "3D ultrafast ultrasound imaging *in vivo*," *Phys. Med. Biol.*, vol. 59, no. 19, pp. L1–L13, Oct. 2014.

[15] E. Roux, F. Varray, L. Petrusca, C. Cachard, P. Tortoli, and H. Liebgott, "Experimental 3-D ultrasound imaging with 2-D sparse arrays using focused and diverging waves," *Sci. Rep.*, vol. 8, no. 1, pp. 1–12, Dec. 2018.

[16] A. Austeng and S. Holm, "Sparse 2-D arrays for 3-D phased array imaging–design methods," *IEEE Trans. Ultrason., Ferroelectr., Freq. Control*, vol. 49, no. 8, pp. 1073–1086, Aug. 2002.

[17] A. Ramalli, E. Boni, E. Roux, H. Liebgott, and P. Tortoli, "Design, implementation, and medical applications of 2-D ultrasound sparse arrays," *IEEE Trans. Ultrason., Ferroelectr., Freq. Control*, early access, Mar. 25, 2022, doi: 10.1109/TUFFC.2022.3162419.

[18] A. Ramalli, E. Boni, A. S. Savoia, and P. Tortoli, "Density-tapered spiral arrays for ultrasound 3-D imaging," *IEEE Trans. Ultrason., Ferroelectr., Freq. Control*, vol. 62, no. 8, pp. 1580–1588, Aug. 2015.

[19] E. Boni, A. C. H. Yu, S. Freear, J. A. Jensen, and P. Tortoli, "Ultrasound open platforms for next-generation imaging technique development," *IEEE Trans. Ultrason., Ferroelectr., Freq. Control*, vol. 65, no. 7, pp. 1078–1092, Jul. 2018.

[20] A. Ortega *et al.*, "A comparison of the performance of different multiline transmit setups for fast volumetric cardiac ultrasound," *IEEE Trans. Ultrason., Ferroelectr., Freq. Control*, vol. 63, no. 12, pp. 2082–2091, Dec. 2016.

[21] A. Ramalli *et al.*, "High-frame-rate tri-plane echocardiography with spiral arrays: From simulation to real-time implementation," *IEEE Trans. Ultrason., Ferroelectr., Freq. Control*, vol. 67, no. 1, pp. 57–69, Jan. 2020.

[22] L. Wei *et al.*, "High frame rate volumetric imaging of microbubbles using a sparse array and spatial coherence beamforming," *IEEE Trans. Ultrason., Ferroelectr., Freq. Control*, vol. 68, no. 10, pp. 3069–3081, Oct. 2021.

[23] A. S. Savoia *et al.*, "A 256-element spiral CMUT array with integrated analog front end and transmit beamforming circuits," in *Proc. IEEE Int. Ultrason. Symp. (IUS)*, Oct. 2018, pp. 206–212.

[24] R. Maffett *et al.*, "Unfocused field analysis of a density-tapered spiral array for High-Volume-Rate 3D ultrasound imaging," *IEEE Trans. Ultrason., Ferroelectr., Freq. Control*, early access, Jul. 4, 2022, doi: 10.1109/TUFFC.2022.3188245.

[25] S. W. Smith, G. E. Trahey, and O. T. von Ramm, "Two-dimensional arrays for medical ultrasound," *Ultrason. Imag.*, vol. 14, no. 3, pp. 213–233, Jul. 1992.

[26] D. H. Turnbull and F. S. Foster, "Fabrication and characterization of transducer elements in two-dimensional arrays for medical ultrasound imaging," *IEEE Trans. Ultrason., Ferroelectr., Freq. Control*, vol. 39, no. 4, pp. 464–475, Jul. 1992.

[27] R. E. Davidsen and S. W. Smith, "Two-dimensional arrays for medical ultrasound using multilayer flexible circuit interconnection," *IEEE Trans. Ultrason., Ferroelectr., Freq. Control*, vol. 45, no. 2, pp. 338–348, Mar. 1998.

[28] M. D. C. Eames and J. A. Hossack, "Fabrication and evaluation of fully-sampled, two-dimensional transducer array for 'sonic window' imaging system," *Ultrasonics*, vol. 48, no. 5, pp. 376–383, Sep. 2008.

[29] D. E. Dausch, K. H. Gilchrist, J. B. Carlson, S. D. Hall, J. B. Castellucci, and O. T. V. Ramm, "*In vivo* real-time 3-D intracardiac echo using PMUT arrays," *IEEE Trans. Ultrason., Ferroelectr., Freq. Control*, vol. 61, no. 10, pp. 1754–1764, Oct. 2014.

[30] T. L. Christiansen, M. F. Rasmussen, J. P. Bagge, L. N. Moesner, J. A. Jensen, and E. V. Thomsen, "3-D imaging using row–column-addressed arrays with integrated apodization—Part II: Transducer fabrication and experimental results," *IEEE Trans. Ultrason., Ferroelectr., Freq. Control*, vol. 62, no. 5, pp. 959–971, May 2015.

[31] D. Wildes *et al.*, "4-D ICE: A 2-D array transducer with integrated ASIC in a 10-Fr catheter for real-time 3-D intracardiac echocardiography," *IEEE Trans. Ultrason., Ferroelectr., Freq. Control*, vol. 63, no. 12, pp. 2159–2173, Dec. 2016.

[32] V. Daeichin *et al.*, "Acoustic characterization of a miniature matrix transducer for pediatric 3D transesophageal echocardiography," *Ultrasound Med. Biol.*, vol. 44, no. 10, pp. 2143–2154, Oct. 2018.

[33] B. D. Lindsey, E. D. Light, H. A. Nicoletto, E. R. Bennett, D. T. Laskowitz, and S. W. Smith, "The ultrasound brain helmet: New transducers and volume registration for *in vivo* simultaneous multi-transducer 3-D transcranial imaging," *IEEE Trans. Ultrason., Ferroelectr., Freq. Control*, vol. 58, no. 6, pp. 1189–1202, Jun. 2011.

[34] H. J. Vos *et al.*, "Sparse volumetric PZT array with density tapering," in *Proc. IEEE Int. Ultrason. Symp. (IUS)*, Oct. 2018, pp. 1–4.

[35] F. Cardarelli, *Materials Handbook*. Cham, Switzerland: Springer, 2018.

[36] B. Hadimioglu and B. T. Khuri-Yakub, "Polymer films as acoustic matching layers," in *Proc. IEEE Symp. Ultrason.*, Dec. 1990, pp. 1337–1340.

[37] E. Boni, F. Fool, M. D. Verweij, H. J. Vos, and P. Tortoli, "On the efficacy of in-probe pre-amplifiers for piezoelectric 2D arrays," in *Proc. IEEE Int. Ultrason. Symp. (IUS)*, Sep. 2020, pp. 1–4.

[38] *0.2 mm Needle Hydrophone (NH0200)*, Precision Acoustics Ltd, Dorchester, U.K., pp. 1–8.

[39] T. L. Szabo, *Diagnostic Ultrasound Imaging: Inside Out*. Amsterdam, The Netherlands: Elsevier, 2014.

[40] A. Ng and J. Swanevelder, "Resolution in ultrasound imaging," *Continuing Educ. Anaesthesia Crit. Care Pain*, vol. 11, no. 5, pp. 186–192, Oct. 2011.

[41] N. Rubert and T. Varghese, "Scatterer number density considerations in reference phantom-based attenuation estimation," *Ultrasound Med. Biol.*, vol. 40, no. 7, pp. 1680–1696, Jul. 2014.

[42] T. Inoue, M. Ohta, and S. Takahashi, "Design of ultrasonic transducers with multiple acoustic matching layers for medical application," *IEEE Trans. Ultrason., Ferroelectr., Freq. Control*, vol. FFC-34, no. 1, pp. 8–16, Jan. 1987.

[43] Z. Li *et al.*, "Broadband gradient impedance matching using an acoustic metamaterial for ultrasonic transducers," *Sci. Rep.*, vol. 7, no. 1, pp. 1–9, Feb. 2017.

[44] S. T. Lau *et al.*, "Multiple matching scheme for broadband $0.72Pb(Mg_{1/3}Nb_{2/3})O_3$–$0.28PbTiO_3$ single crystal phased-array transducer," *J. Appl. Phys.*, vol. 105, no. 9, May 2009, Art. no. 094908.

Luxi Wei (Member, IEEE) received the B.Sc. degree (Hons.) in biophysics from The University of British Columbia, Vancouver, BC, Canada, in 2016, and the M.Sc. degree in medical biophysics from the University of Toronto, Toronto, ON, Canada, in 2019. She is currently pursuing the Ph.D. degree with the Department of Biomedical Engineering, Erasmus Medical Center, Rotterdam, The Netherlands.

Her research includes high frame rate ultrasound, contrast agent imaging, volumetric imaging, and transducer development.

Enrico Boni (Senior Member, IEEE) was born in Florence, Italy, in 1977. He received the M.Sc. degree in electronic engineering from the University of Florence, Florence, in 2001, and the Ph.D. degree in electronic system engineering from the University of Florence, in 2005.

Since 2021, he has been an Associate Professor in electronics with the Department of Information Engineering, University of Florence. His research interests include analog and digital systems design, digital signal processing algorithms, digital control systems, Doppler ultrasound (US) signal processing, microemboli detection and classification, US research platforms, and US front-end electronics design.

Alessandro Ramalli (Senior Member, IEEE) was born in Prato, Italy, in 1983. He received the master's degree in electronics engineering from the University of Florence, Florence, Italy, in 2008, and the joint Ph.D. degree in electronics system engineering and automation, systems and images from the University of Florence and the University of Lyon, Lyon, France, respectively, in 2012.

From 2012 to 2017, he was involved in the development of the imaging section of a programmable open ultrasound (US) system by the University of Florence. From 2017 to 2019, he was a Postdoctoral Researcher with the Laboratory of Cardiovascular Imaging and Dynamics, KU Leuven, Leuven, Belgium, granted by the European Commission through a "Marie Skłodowska-Curie Individual Fellowships." Here, he developed high frame rate imaging techniques for echocardiography. From 2020 to 2022, he was a Research Fellow with the University of Florence, where he is currently an Assistant Professor. His research interests include medical imaging, echocardiography, beamforming methods, US simulation, and arrays and systems design.

Fabian Fool (Graduate Student Member, IEEE) received the B.Sc. and M.Sc. degrees (*cum laude*) in applied physics from the Delft University of Technology, Delft, The Netherlands, in 2015 and 2017, respectively. He is currently pursuing the Ph.D. degree with the Laboratory of Acoustical Wavefield Imaging, Delft University of Technology, where he is involved in designing matrix transducers and imaging strategies for various applications.

His research interests include beamforming algorithms and transducer design.

Emile Noothout received the Diploma degree from the Intermediate Technical School for Mechanics, Dordrecht, The Netherlands, in 2004.

From 2004 to 2006, he was with the Leidse Instrumentmaker School, Leiden, The Netherlands, where he studied for Research Instrument Maker. From 2007 to 2013, he was a Research Instrument Maker with TNO, Delft, The Netherlands, where he developed hardware for space and lithography. Since 2008, he has been involved in developing and building ultrasound (US) transducers for the petrochemical industries. Since 2013, he has been with the Delft University of Technology, Delft, where he is involved in the development of medical US transducers and research assistance.

Antonius F. W. van der Steen (Fellow, IEEE) received the M.Sc. degree in applied physics from Technical University Delft, Delft, The Netherlands, in 1989, and the Ph.D. degree in medical science from Catholic University Nijmegen, Nijmegen, The Netherlands, in 1994.

He is currently the Head of biomedical engineering with the Thorax Center, Erasmus MC, Rotterdam, The Netherlands. He is an expert in ultrasound, cardiovascular imaging, and cardiovascular biomechanics. He has a career at the crossroads of engineering, health care, and industry. He was the Co-PI of ParisK, one of the large CTMM projects (16 MEuro). His international profile is high, with more than 200 invited lectures all over the world, and Guest Professorship/Guest Researcher in Canada, Japan, and China.

Dr. van der Steen is a fellow of the European Society of Cardiology. He is a member of the Netherlands Academy of Technology (AcTI) and a Board Member of the Royal Netherlands Academy of Sciences (KNAW). He was a recipient of the Simon Stevin Master Award and the NWO PIONIER Award in Technical Sciences. He has experience in running large consortia as the Co-Founder and former Chairman of the Medical Delta, which comprises of over 280 scientists working on technical solutions for sustainable health.

Martin D. Verweij (Member, IEEE) received the M.Sc. degree (*cum laude*) and the Ph.D. degree in electrical engineering from the Delft University of Technology, Delft, The Netherlands, in 1988 and 1992, respectively.

From 1993 to 1997, he was a Research Fellow with the prestigious Royal Netherlands Academy of Arts and Sciences, Amsterdam, The Netherlands. In 1995 and 1997, he joined Schlumberger Cambridge Research, Cambridge, U.K., as a Visiting Scientist. In 1998, he joined the Laboratory of Electromagnetic Research, Delft University of Technology, as an Assistant Professor, and later that year as an Associate Professor. In 2011, he switched to the Laboratory of Medical Imaging, Delft University of Technology, where he became the Head of Ultrasound Research, in 2021. Since 2015, he has a part-time position at the Biomedical Engineering Group, Erasmus Medical Center, Rotterdam, The Netherlands. He is the originator of the Iterative Nonlinear Contrast Source (INCS) method for the computation of nonlinear US fields. His research interests include dedicated transducer design, beamforming algorithms, the mathematical modeling and numerical simulation of ultrasound (US), and the physics of US.

Dr. Verweij is a Research Leader of the Dutch Technology Foundation (TTW-NWO) on projects involving transducer design, beamforming, and imaging. He is a fellow of the Acoustical Society of America, an Associate Editor of the *Journal of the Acoustical Society of America*, and Treasurer of the Dutch Society for Medical Ultrasound.

Piero Tortoli (Life Fellow, IEEE) received the Laurea degree in electronics engineering from the University of Florence, Florence, Italy, in 1978.

Since then, he has been the Faculty of the Information Engineering Department, University of Florence, where he is currently a Full Professor of electronics. He is leading the Microelectronics Systems Design Laboratory. His research interests include the development of open ultrasound research systems and novel imaging/Doppler methods. On these topics, he has authored more than 300 articles.

Mr. Tortoli is a fellow of AIMBE, "Docteur Honoris causa" of the University Claude Bernard Lyon 1, and an Honorary Member of the Polish Academy of Sciences. He was elected as a member of the Academic Senate. He has been served on the IEEE International Ultrasonics Symposium Technical Program Committee since 1999 and was an Associate Editor and a Guest Editor of three special issues for the IEEE TRANSACTIONS ON ULTRASONICS, FERROELECTRICS, AND FREQUENCY CONTROL (from 2012 to 2022). He chaired the 22nd International Symposium on Acoustical Imaging (1995) and the 12th New England Doppler Conference (2003), established the Artimino Conference on Medical Ultrasound Technology in 2011, and organized it again in 2017.

Nico de Jong (Member, IEEE) received the M.Sc. degree in applied physics in the field of pattern recognition from the Delft University of Technology, Delft, The Netherlands, in 1978, and the Ph.D. degree from Erasmus University, Rotterdam, The Netherlands, in 1993, with the thesis "acoustic properties of ultrasound contrast agents."

From 2003 to 2011, he was a part-time Professor with the Group Physics of Fluids headed by Prof. Detlef Lohse, University of Twente, Enschede, The Netherlands. He is currently the Vice Head of biomedical engineering with the Thoraxcenter, Erasmus University Medical Center, Rotterdam, The Netherlands, headed by Prof. Ton van der Steen. He is the Head of the Medical Imaging Group, Technical University, Delft. He teaches on Technical Universities and the Erasmus MC. He has graduated 38 Ph.D. students and is currently supervising more than 12 Ph.D. students.

Dr. Jong is the Founder and an Organizer of the Annual European Symposium (this year for the 25th time, see http://www.echocontrast.nl) on US contrast imaging, held in Rotterdam and attended by approximately 175 scientists from universities and industries all over the world. He is on the safety committee of the World Federation of Ultrasound in Medicine and Biology (WFUMB). He is an Associate Editor of *Ultrasound in Medicine and Biology* and the IEEE TRANSACTIONS ON ULTRASONICS, FERROELECTRICS, AND FREQUENCY CONTROL. He has been a Guest Editor for special issues of several journals.

Hendrik J. Vos (Member, IEEE) received the M.Sc. degree in applied physics from the Delft University of Technology, Delft, The Netherlands, in 2004, and the Ph.D. degree from the Department of Biomedical Engineering, Erasmus MC, Rotterdam, The Netherlands, in 2010.

He was a Postmaster Researcher with the University of Florence, Florence, Italy, and as a Contract Researcher for the petrochemical industry on cutting-edge ultrasonic solutions. He is currently an Associate Professor with Erasmus MC and Delft University of Technology. His research interests include acoustical array technology for biomedical imaging in all its aspects: transducers, 2-D and 3-D beamforming, cardiac shear waves, ultrafast Doppler, contrast imaging, and related subclinical and clinical studies.

Dr. Vos received a Dutch NWO-TTW-VIDI Personal Grant in 2018.